



# Regulating the electronic property of iron catalysts for higher alcohols synthesis from CO<sub>2</sub> hydrogenation

Ruwei Yao<sup>a</sup>, Bin Wu<sup>a</sup>, Yang Yu<sup>b</sup>, Na Liu<sup>b</sup>, Qinqin Niu<sup>a</sup>, Congming Li<sup>a,\*</sup>, Jian Wei<sup>b,\*</sup>, Qingjie Ge<sup>b,\*</sup>

<sup>a</sup> State Key Laboratory of Clean and Efficient Coal Utilization, Taiyuan University of Technology, Taiyuan 030024, China

<sup>b</sup> Dalian National Laboratory for Clean Energy, Dalian Institute of Chemical Physics, Chinese Academy of Sciences, Dalian 116023, China

## ARTICLE INFO

### Keywords:

CO<sub>2</sub> hydrogenation  
Higher alcohols  
Iron  
Sulfate  
Alkali metal

## ABSTRACT

The electronic property of a catalyst is crucial to the generation of key reaction intermediates for targeted synthesis. Herein, we reported a strategy by modifying iron catalysts with sulfate and alkali metal (Li, Na, or K) to regulate the electronic property and optimize the reaction pathways for CO<sub>2</sub> hydrogenation to higher alcohols. The characterizations demonstrated the influencing relationship between the electronic property of iron catalysts and the catalytic capabilities for CO dissociation, non-dissociated CO activation and catalytic hydrogenation, which were critical to selective synthesis of higher alcohols. Na-S modification was proven more effective to balance the multiple capabilities required for higher alcohols synthesis and the NaS-Fe catalyst gave a higher C<sub>2+</sub>OH yield in CO<sub>2</sub> hydrogenation. DFT calculations further validated the advantage of Na-S modification from the aspects of CO adsorption and C–C coupling. This strategy provides more flexibility in site regulation and applies to catalyst design for many reactions.

## 1. Introduction

Under the dual pressures of rapidly depleting fossil fuels and increasing carbon emissions, using CO<sub>2</sub> as a carbon source to produce fuels and chemicals through catalytic hydrogenation has emerged as a promising strategy for closing the carbon cycle and achieving sustainable development [1–4]. Directly converting CO<sub>2</sub> into C<sub>2+</sub> oxygenates, particularly higher alcohols, has attracted considerable interest due to its higher atomic utilization efficiency and wide application as solvents and fuel additives [5–8]. Higher alcohols synthesis (HAS) from CO<sub>2</sub> hydrogenation usually follows CO-mediated pathway, in which the non-dissociated CO species insert into the alkyl species generated from CO dissociation to form C<sub>2+</sub> alcohols [9,10]. The formation of higher alcohols is not favored in CO<sub>2</sub> hydrogenation due to the higher thermodynamic and kinetic barriers compared to the formation of hydrocarbons [11]. Optimizing the balance between catalytic sites for dissociated and non-dissociated CO activation, as well as enhancing the synergy between these sites, has been proven to accelerate the key step of alkyl–\*CO coupling and boost the production of higher alcohols [12, 13]. Different active metals (such as Fe and Cu) are generally applied in HAS catalysts to cover the functions for dissociated and non-dissociated

CO activation [14–16], and various promoters and supports are also used to regulate the catalytic property of metal sites and enhance the synergy for alcohol formation [17–19]. However, the reported HAS catalysts generally demonstrate low selectivity and yield for higher alcohols, which hinders their suitability for industrial applications. Moreover, rapid deactivation of composite metallic catalysts is inevitable due to the phase separation during reaction process and the resulting weak synergy [20]. The challenge for catalyst development continues to be creating the catalytic sites necessary for HAS and maintaining effective synergy featuring the successive reaction steps.

The metal Fe is well-studied in CO<sub>2</sub> hydrogenation due to its high activity in both reverse water-gas shift (RWGS) reaction and Fischer-Tropsch synthesis (FTS), and is often used as an active component in HAS catalysts [21]. Alkali metals such as Na or K are extensively applied to modify iron catalysts and have been proven effective in improving CO<sub>2</sub>/CO dissociation and C–C coupling to C<sub>2+</sub> products [22]. Designing active sites for non-dissociated CO activation on this basis is a viable approach to boost alcohol formation on iron-based catalysts. Generally, activation behavior of the adsorbed CO species correlates with the electronic environment of metal sites [23]. Based on the above considerations, we proposed the strategy of alkali metal and sulfate

\* Corresponding authors.

E-mail addresses: [licongming0523@163.com](mailto:licongming0523@163.com) (C. Li), [weijian@dicp.ac.cn](mailto:weijian@dicp.ac.cn) (J. Wei), [geqj@dicp.ac.cn](mailto:geqj@dicp.ac.cn) (Q. Ge).

<https://doi.org/10.1016/j.apcatb.2024.124159>

Received 27 March 2024; Received in revised form 26 April 2024; Accepted 4 May 2024

Available online 8 May 2024

0926-3373/© 2024 Elsevier B.V. All rights reserved.

co-modification to regulate the electronic property of iron catalyst and enhance the ability for non-dissociated CO activation. The presence of sulfate, with electron-withdrawing property, could decrease the electronic density of the surrounding Fe sites and reduce their ability to return electrons to the C–O bond. Then the function of part of Fe sites was expected to switch from CO dissociation to non-dissociated CO activation, leading to a better balance required for HAS [24]. Furthermore, the method of modifying a monometallic iron catalyst with limited electronic promoters can create the required sites within a single metal phase, thereby circumventing the issue of phase separation during the reaction.

Following this strategy, the iron catalysts modified with sulfate and an alkali metal (Li, Na, or K) were prepared and tested for CO<sub>2</sub> hydrogenation to higher alcohols. The influence of applied dual-promoter on phase transformation and electronic property of iron catalysts, along with the significance of these difference for catalytic activity and selectivity, were investigated. The results suggested that the surface activation behavior towards CO<sub>2</sub>/H<sub>2</sub> reactants and CO intermediates varied with the promoters, due to the different electronic effects, which consequently affected the dominant reactive species and reaction pathways. The alkali metal Na, in combination with sulfate, was proven feasible in balancing the alkyl, \*CO and \*H species on iron catalyst during the reaction, which was more favorable for HAS based on CO-mediated pathway. The advantage of Na-S, as compared to Li-S and K-S modification, stemmed from the effective and moderate electronic effects of Na. Clearly, the combination of sulfate with alkali metal expands the regulatory range of the catalytic property of iron catalysts. This knowledge is useful for the development of catalysts with multiple promoters, not only for CO<sub>x</sub> hydrogenation reactions, but also for other reactions that are sensitive to the electronic environment of metal sites.

## 2. Experimental section

### 2.1. Catalyst preparation

The alkali metal (AM) and sulfate co-modified iron catalysts were prepared via precipitation/washing method using Fe<sub>2</sub>(SO<sub>4</sub>)<sub>3</sub> as iron source, hydroxide of alkali metal (LiOH, NaOH, or KOH) as precipitating agent. Typically, Fe<sub>2</sub>(SO<sub>4</sub>)<sub>3</sub>·xH<sub>2</sub>O were dissolved in a mixture of 150 mL of deionized water and 0.8 mL of 18.4 mol L<sup>-1</sup> H<sub>2</sub>SO<sub>4</sub>. Then, 1.5 mol L<sup>-1</sup> AMOH was added dropwise in the mixture under constant stirring at 60 °C, until reaching a pH of 10. The obtained suspension was aged for another 1 h, followed by centrifugation and washing. After drying at 80 °C for 12 h, the precursors were calcined at 400 °C for 2 h. The obtained catalysts using different precipitating agent were denoted as Li-S-Fe, Na-S-Fe and K-S-Fe, respectively. The catalysts were modified simultaneously with the residual alkali metal and sulfate, without any extra addition. The contents of alkali metal and S in the catalysts were carefully controlled by altering the amount of deionized water during washing process, and the specific contents were given in Table S1.

### 2.2. Catalyst evaluation

CO<sub>2</sub> hydrogenation reactions were carried out in a stainless fixed-bed reactor. Typically, the catalyst was pre-reduced in situ in H<sub>2</sub> flow at 350 °C for 8 h, and then cooled down to 280 °C. Subsequently, the reactor was pressurized to 3.0 MPa with the reactant gas (H<sub>2</sub>/CO<sub>2</sub>/N<sub>2</sub> = 72/24/4), following by increasing the system temperature to 320 °C. The condition of 320 °C, 3.0 MPa, and 8000 mL g<sub>cat</sub><sup>-1</sup> h<sup>-1</sup> was maintained during the reaction process. The effluent was analyzed online by a gas chromatograph (GC-Agilent 7890B) with flame ionization detector (FID) and PONA capillary column. N<sub>2</sub>, CO, CH<sub>4</sub> and CO<sub>2</sub> were then analyzed by another GC system (GC-2014AT, SHIMADZU) with thermal conductivity detector (TCD) and TDX-01 packed column. The connecting pipe between the reactor and GC were heated to 160 °C to avoid product condensation. A cold trap was placed before entering the TCD detector

to remove water and heavy products.

### 2.3. Catalyst characterization

X-ray power diffraction (XRD) patterns were collected to identify the phases and crystallinity on a PANalytical X'Pert Pro diffractometer with Cu Kα radiation at 60 kV and 55 mA. Transmission electron microscopy (TEM) images were obtained with a TECNAI G2 F20 system at 200 kV. The Brunauer-Emmett-Teller (BET) surface areas of the catalysts were determined by N<sub>2</sub> sorption operated at 77 K using a QuantaChrome Quadrasorb SI instrument, and the catalysts were degassed at 300 °C for 5 h under vacuum before measurement. The element analysis (S, Li, Na, K) of the catalysts was conducted on an inductively coupled plasma optical emission spectrometer (ICP-OES, PerkinElmer 7300DV). X-ray photoelectron spectroscopy (XPS) characterization was carried out on a Thermo ESCALAB 250XI spectrometer using Al Kα radiation. The binding energies were calibrated by the C1s peak at 284.8 eV. The Mössbauer spectra (MES) of spent catalysts were recorded under room temperature on Topologic 500 A spectrometer, with <sup>57</sup>Co (Rh) moving in a constant acceleration mode as the radioactive source. Unless otherwise specified, the catalysts after 8 h of reaction were used for the characterizations of spent catalysts.

Temperature-programmed reduction with H<sub>2</sub> (H<sub>2</sub>-TPR) was conducted on a Micromeritics AutoChem 2910 apparatus. The catalyst was pretreated in Ar flow at 300 °C for 30 min, and then cooled down to ambient temperature. Afterward, the catalyst temperature was ramped up to 900 °C at a rate of 10 °C/min in 10 % H<sub>2</sub>/Ar, with the H<sub>2</sub> consumption monitored by a thermal conductivity detector (TCD).

Temperature-programmed desorption with CO<sub>2</sub> (CO<sub>2</sub>-TPD) was conducted on a Micromeritics AutoChem 2910 apparatus. After the reduction treatment in H<sub>2</sub> flow at 350 °C for 3 h, the catalyst was cooled down to 50 °C. The catalyst was then saturated in CO<sub>2</sub> flow for 30 min, and purged with flowing He gas until the baseline was steady. Finally, the catalyst temperature was ramped from 50 °C to 900 °C at a rate of 10 °C/min in He flow, with the CO<sub>2</sub> (*m/z* = 44) and CO (*m/z* = 28) signals recorded by an online mass spectrometer.

C<sub>3</sub>H<sub>6</sub> pulse transient hydrogenation experiments were performed on spent catalysts. The sample was pre-treated in H<sub>2</sub> flow at 350 °C for 2 h to reduce the passivated surface, and the system temperature was then maintained at 50 °C. Afterward, H<sub>2</sub> acted as carrier gas, and 5 % C<sub>3</sub>H<sub>6</sub>/95 % Ar was pulsed into the system for several cycles, during which the transient response signals of C<sub>3</sub>H<sub>6</sub> (*m/z* = 42), C<sub>3</sub>H<sub>8</sub> (*m/z* = 44) and CH<sub>4</sub> (*m/z* = 15) were monitored by an online mass spectrometer.

In situ XRD patterns were collected by an Empyrean-100 PANalytical diffractometer with Cu Kα radiation at 40 kV and 40 mA. During the reduction process, the sample was heated from room temperature to 350 °C (5 °C/min) in 50 % H<sub>2</sub>/50 % N<sub>2</sub> flow and then maintained at 350 °C for 4 h. After cooling to 320 °C naturally, the reactant gas (H<sub>2</sub>/CO<sub>2</sub> = 3) was introduced into the system and maintained for 2 h. All the treatments were performed under atmospheric pressure.

In situ diffuse reflectance infrared Fourier transform spectroscopy (DRIFTS) of CO adsorption was performed on a PerkinElmer Frontier spectrometer. The spent samples were pre-treated in H<sub>2</sub> flow at 350 °C for 1 h, and then flushed by Ar for 30 min. The system temperature was then cooled down to 50 °C and maintained, meanwhile, the background was collected. Afterward, the sample was saturated with CO for 30 min, and the spectra were collected every 5 min under Ar flow purging.

In situ high-pressure DRIFTS of CO<sub>2</sub> hydrogenation reaction was conducted on a PerkinElmer Frontier spectrometer. The sample was in situ reduced in H<sub>2</sub> flow at 350 °C for 8 h and then flushed by Ar for 30 min. After the reaction cell cooling down to 320 °C, the background was collected. The reduced sample was then treated with reactant gas (H<sub>2</sub>/CO<sub>2</sub>/N<sub>2</sub> = 72/24/4, 20 mL/min) at 320 °C and 1.0 MPa for 1 h, and the spectra were concurrently collected.

The spin-polarized DFT calculations were performed using the projector augmented wave (PAW) method, the generalized gradient

approximation (GGA) in the form of Perdew-Burke-Ernzerhof for the exchange-correlation potentials, and a plane-wave basis set with an energy cutoff of 450 eV, as implemented in the Vienna ab initio simulation package (VASP). The van der Waals interaction was taken into account at DFT-D3 level. Given structural models were relaxed until the Hellmann-Feynman forces smaller than 0.02 eV/Å and the change in energy smaller than  $10^{-5}$  eV was attained. The adsorption energy of \*CO was calculated according to  $E_{\text{ads}} = E_{\text{TOT}} - E_{\text{slab}} - E_{\text{CO}}$ , where  $E_{\text{TOT}}$  is the total energy of the slab with \*CO,  $E_{\text{slab}}$  is the total energy of the bare slab, and  $E_{\text{CO}}$  is the total energy of the free CO in the gas phase. Transition state search of C–C coupling process between CO and CH<sub>2</sub> using NEB method to obtain coupling energy barrier. The barrier ( $E_a$ ) and reaction energy ( $\Delta E$ ) are calculated according to  $E_a = E_{\text{TS}} - E_{\text{IS}}$  and  $\Delta E = E_{\text{FS}} - E_{\text{TS}}$ , where  $E_{\text{IS}}$ ,  $E_{\text{TS}}$  and  $E_{\text{FS}}$  are the energies of the corresponding initial state (IS), transition state (TS) and final state (FS), respectively. The Fe<sub>5</sub>C<sub>2</sub>(510) facet was selected to investigate the surface reaction.

### 3. Results and discussion

#### 3.1. Catalytic performance of HAS

A series of iron catalysts modified with alkali metal and sulfate were evaluated in CO<sub>2</sub> hydrogenation under a condition of 320 °C, 3.0 MPa, H<sub>2</sub>/CO<sub>2</sub> = 3, and 8000 mL g<sub>cat</sub><sup>−1</sup> h<sup>−1</sup>. As expected, CO<sub>2</sub> conversion and product selectivity varied with the type and content of promoters in the catalyst (Fig. S1, Table S2). The most active Li-S, Na-S, and K-S promoted iron catalysts in alcohol productivity screening, were chosen for a more detailed study of the influence of dual-promoter on alcohol formation. Fig. 1a displayed the catalytic performance of CO<sub>2</sub>

hydrogenation over the selected LiS-Fe, NaS-Fe, KS-Fe, and pure Fe catalysts. Note that the selected NaS-Fe and KS-Fe catalysts possessed similar promoter contents, with 2.4 wt% Na and 0.6 wt% S in NaS-Fe and 3.0 wt% K and 0.6 wt% S in KS-Fe. The Li-S modified iron catalyst with similar promoter content demonstrated undetectable activity for CO<sub>2</sub> hydrogenation, and both the contents of Li and S in the selected LiS-Fe were less than 0.3 wt%. In terms of performance, CO<sub>2</sub> conversion increased significantly from 25.5 % to 37.1 % with increasing atomic number of the applied alkali metal (Li-S→Na-S→K-S), accompanied by a decrease in CO selectivity from 22.6 % to 12.6 %. This suggested that the presence of heavier alkali metal was more conducive to CO<sub>2</sub> activation and a further conversion of the generated CO species.

CO species are considered to be important reaction intermediates during CO<sub>2</sub> hydrogenation, and the opposite trend for CO<sub>2</sub> conversion and CO selectivity with varying reaction conditions also supported this point (Fig. S2). The conversion tendency of adsorbed CO species would affect the generation of reactive species and determine the dominant pathways in the complex reaction network [18]. Obviously, the conversion pathway of CO intermediates differed by the dual-promoter in the iron catalyst. Light alkanes, especially methane (48.6 %), were the dominant products on LiS-Fe catalyst, which was almost the same as the pure Fe catalyst without any modification, and the selectivity to C<sub>2</sub>+ alcohols (C<sub>2</sub>+OH) was only 0.9 %. This suggested the alkyl species generated from CO dissociation were readily hydrogenated into alkanes on LiS-Fe catalyst, rather than participating in C–C coupling reactions. C–C coupling and hydrogenated termination are competing reactions, and an efficient HAS catalyst is required to inhibit or severely reduce the hydrogenation steps, which are thermodynamically more favorable [25–28]. Clearly, Li-S dual-promoter was insufficient for effective

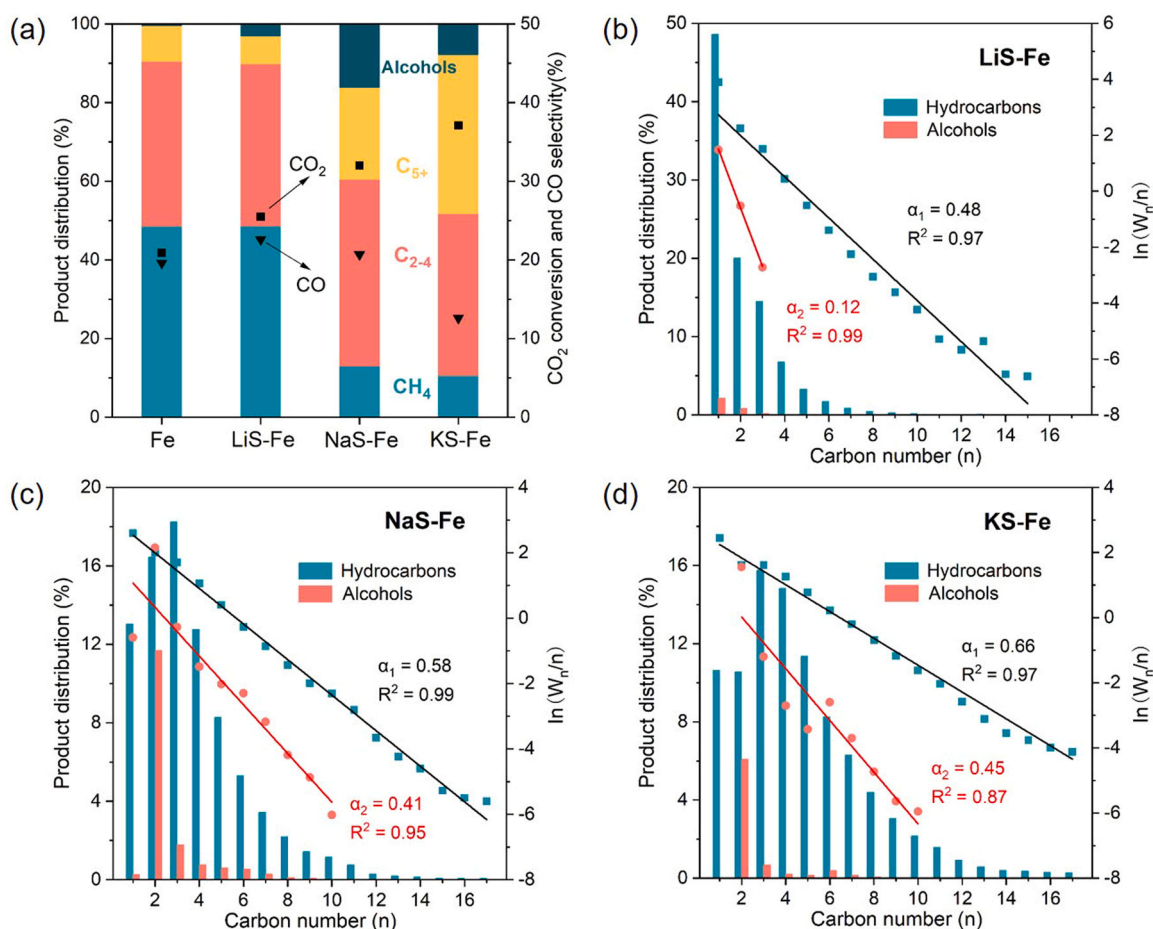


**Fig. 1.** (a) Conversion and product selectivity of iron catalysts in CO<sub>2</sub> hydrogenation. ASF distributions of hydrocarbon and alcohol products over (b) LiS-Fe, (c) NaS-Fe, and (d) KS-Fe catalysts. Reaction conditions: 320 °C, 3.0 MPa, H<sub>2</sub>/CO<sub>2</sub> = 3, and 8000 mL g<sub>cat</sub><sup>−1</sup> h<sup>−1</sup>, time on stream of 8 h.



hydrogenation inhibition. Generally, Na and K are more common in Fe-based catalysts for CO<sub>x</sub> hydrogenation due to their positive role in inhibiting hydrogenation and promoting C–C coupling [29–31]. The formation of methane was significantly inhibited on NaS-Fe and KS-Fe catalysts, and the selectivity to long-chain hydrocarbons (C<sub>5+</sub>) got a substantial increase. Besides, the heavier alkali metal seemed more conducive to chain growth as indicated by the highest C<sub>5+</sub> selectivity for KS-Fe catalyst.

With regard to the alcohol products, NaS-Fe catalyst exhibited the highest C<sub>2+</sub>OH selectivity (15.9 %) with a CO<sub>2</sub> conversion of 32.0 % among the studied catalysts. Na-S dual-promoter should function better in optimizing the balance between the active sites required for HAS as compared with Li-S and K-S. The yield of C<sub>2+</sub>OH reached 78.5 mg g<sub>cat</sub><sup>−1</sup> h<sup>−1</sup> at relatively mild condition, which was an extension of what we think is difficult to achieve with a monometallic iron catalyst (Table S3). Iron is active in CO dissociation and generally contributes to the formation of hydrocarbons [32,33]. In addition, the detailed distributions of hydrocarbon and alcohol products over the catalysts are given as well (Fig. 1b–d). Both the hydrocarbon and alcohol products basically followed the Anderson-Schulz-Flory (ASF) distribution, confirming the similar pathway via CO intermediate. The chain growth probability for hydrocarbons ( $\alpha_1$ ) exceeded that for alcohols ( $\alpha_2$ ) over the LiS-Fe (0.48 vs. 0.12), NaS-Fe (0.58 vs. 0.41) and KS-Fe (0.66 vs. 0.45) catalysts, in line with the fact that the rate of alkyl–\*CO coupling was lower than that of alkyl–alkyl coupling due to the thermodynamic and kinetic barriers [15]. Note that the gap between the  $\alpha$  values for alcohols and hydrocarbons on NaS-Fe catalyst (0.17) was smaller compared to KS-Fe (0.21) and LiS-Fe (0.36) catalysts, suggesting that Na-S dual-promoter could play a better role in balancing alkyl and \*CO species on the catalyst surface and accelerating the rate of alkyl–\*CO coupling dynamically. Moreover, the distribution of organic products was less sensitive to reaction conditions (Fig. S2), and the C<sub>2+</sub>OH selectivity on NaS-Fe catalyst was basically stable over 50 h on stream (Fig. S3), providing the possibility to achieve stable production of higher alcohols for industrial applications.

### 3.2. Textural properties

The textural properties of LiS-Fe, NaS-Fe and KS-Fe catalysts were characterized by XRD and TEM. The XRD patterns in Fig. 2a suggested that the catalysts were stabilized in the form of Fe<sub>2</sub>O<sub>3</sub> phase, and the peak intensities decreased with increasing atomic number of the alkali

metal, associated with a decrease in catalyst crystallinity. No diffraction peaks related to alkali metals and sulfur were observed due to the low contents. The TEM images in Fig. 2b showed that both NaS-Fe and KS-Fe catalysts were integrated by irregular rod-shaped nanoparticles with an average length of 47–52 nm, while LiS-Fe catalyst was composed of sphere-shaped nanoparticles with an average diameter of 34 nm. The difference in morphology and size was likely due to the radius of alkali metal ions and their interaction with Fe. The lattice fringes with 0.22, 0.27, and 0.36 nm interspace were observed in the high-resolution TEM (HRTEM) images, corresponding to the (113), (104) and (012) planes of Fe<sub>2</sub>O<sub>3</sub>, respectively. In addition, the surface area and pore distribution of the catalysts were analyzed by N<sub>2</sub> physisorption (Fig. S4, Table S4). The samples displayed type-IV sorption isotherms typically associated with the presence of mesopores, and the mesopores were attributed to the voids between the aggregated nanoparticles. The specific surface areas of LiS-Fe, NaS-Fe and KS-Fe catalysts were determined to be 37, 52, and 69 m<sup>2</sup> g<sup>−1</sup>, respectively, and the variation was in accordance with the decrease in catalyst crystallinity.

### 3.3. Surface activation behaviors

The adsorption and activation behaviors of CO<sub>2</sub>/H<sub>2</sub> reactants and CO intermediate on catalyst surface are critical to the reaction network for targeted product synthesis. H<sub>2</sub>-TPR was first performed to study the interaction of H<sub>2</sub> with the iron catalysts (Fig. 3a). The H<sub>2</sub> consumption peaks in the range of 250–400 °C were mainly attributed to the reduction of Fe<sub>2</sub>O<sub>3</sub> to Fe<sub>3</sub>O<sub>4</sub>, and the broad peaks above 400 °C corresponded to the subsequent reduction to metallic Fe [6]. The TPR curve of NaS-Fe was quite similar to that of KS-Fe, and the effects of Na-S and K-S modification on H<sub>2</sub> activation and catalyst reducibility were expected to be similar. Regarding the H<sub>2</sub> consumption peaks in low-temperature region (< 400 °C), H<sub>2</sub> dissociation and hydrogenation steps seemed easier on LiS-Fe catalyst in this temperature range as reflected by the peak positions. A stronger hydrogenation tendency was to be expected for LiS-Fe catalyst under a reaction temperature of CO<sub>2</sub> hydrogenation. As for the significantly broadened main reduction peak for LiS-Fe, the massive enrichment of Li on the catalyst surface may be the key factor hindering the reduction process, as reflected by the XPS elemental analysis (Table S5). The surface atomic ratio of Li on LiS-Fe catalyst reached up to 80 %. In addition, pulse transient experiments using C<sub>3</sub>H<sub>6</sub> as the probe molecule were performed on spent catalysts to investigate the difference in hydrogenation ability (Fig. 3b–d). The LiS-Fe catalyst

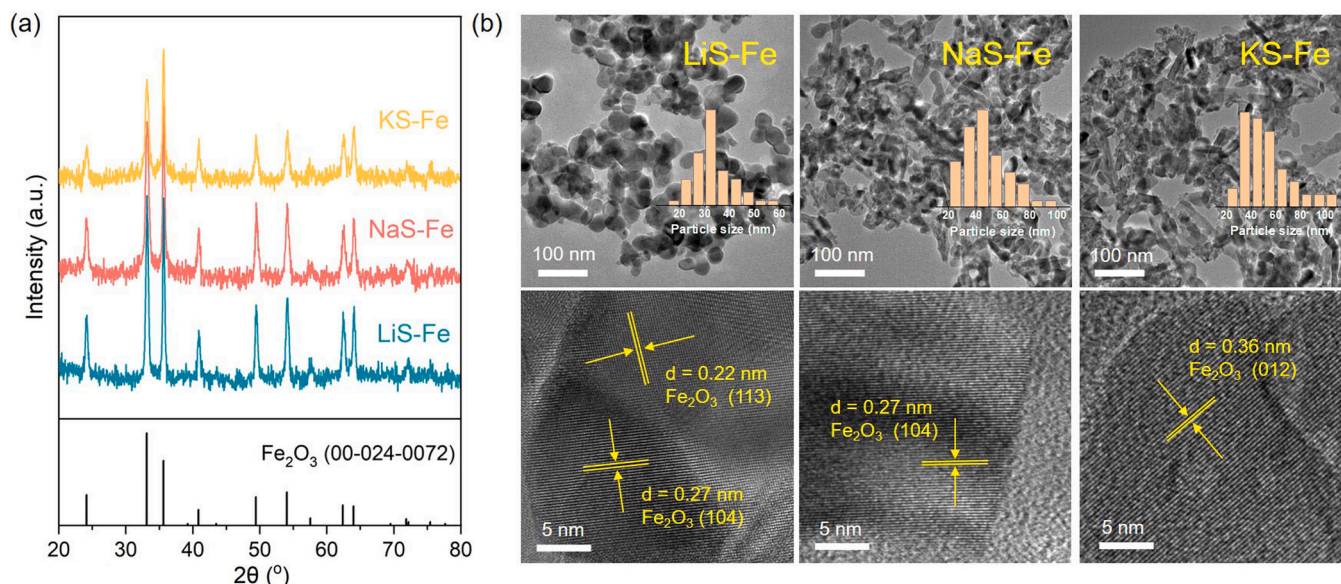


Fig. 2. Structural characterizations of fresh catalysts. (a) XRD patterns. (b) TEM (above) and corresponding HRTEM (below) images.



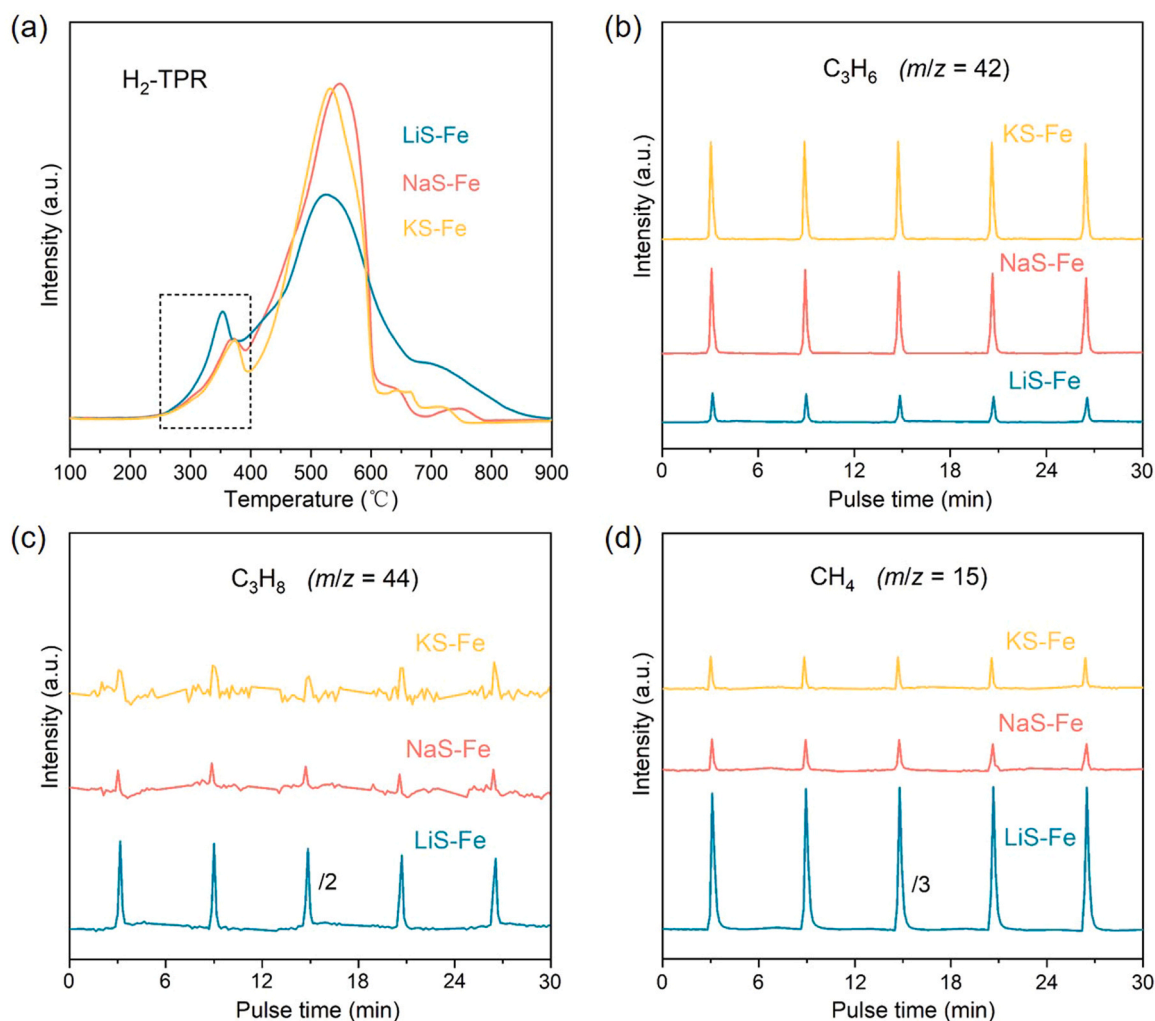


Fig. 3. (a) H<sub>2</sub>-TPR profiles. MS signals of (b) C<sub>3</sub>H<sub>6</sub>, (c) C<sub>3</sub>H<sub>8</sub>, and (d) CH<sub>4</sub> during C<sub>3</sub>H<sub>6</sub> pulse experiments.

showed much lower intensity of C<sub>3</sub>H<sub>6</sub> signals and much higher intensity of C<sub>3</sub>H<sub>8</sub> signals compared to the NaS-Fe and KS-Fe catalysts. Clearly, C<sub>3</sub>H<sub>6</sub> was easily re-adsorbed on LiS-Fe catalyst and hydrogenated to the corresponding alkane, verifying the stronger hydrogenation tendency. Note that obvious CH<sub>4</sub> signals were also detected during C<sub>3</sub>H<sub>6</sub> pulse experiments, and the peak intensity on LiS-Fe was almost two orders of magnitude larger than that of NaS-Fe and KS-Fe catalysts. This indicated that the LiS-Fe catalyst had strong ability to hydrocrack the re-adsorbed C<sub>3</sub>H<sub>6</sub> into CH<sub>4</sub>, which provided further evidence of the much lower olefin selectivity and higher CH<sub>4</sub> selectivity during CO<sub>2</sub> hydrogenation [34,35]. Based on the similar high intensity of C<sub>3</sub>H<sub>6</sub> signals and weak intensity of C<sub>3</sub>H<sub>8</sub> and CH<sub>4</sub> signals on NaS-Fe and KS-Fe catalysts, the initially produced olefins during CO<sub>2</sub> hydrogenation tended to desorb from the catalyst surface, rather than being re-adsorbed and hydrogenated to alkanes. Hydrogenation reactions, as competing steps, need to be inhibited for the efficient synthesis of higher alcohols. Using Na or K as a promoter is more effective in meeting this requirement.

The impact of the dual-promoters was also reflected in the interaction of CO<sub>2</sub> reactant with the catalyst surface through altering surface basicity. In CO<sub>2</sub>-TPD profiles (Fig. 4a), the CO<sub>2</sub> desorption peaks below 400 °C were mainly ascribed to the physically adsorbed and weakly chemisorbed CO<sub>2</sub> molecules, while the desorption peaks above 400 °C corresponded to the strongly adsorbed CO<sub>2</sub> with the basic sites on catalyst surface [19,32]. Only weak CO<sub>2</sub> adsorption was observed on LiS-Fe catalyst, which was evidence for its lower CO<sub>2</sub> conversion during reaction. The carburization process during CO<sub>2</sub> hydrogenation should

also be hindered due to the weak CO<sub>2</sub> adsorption [36]. In contrast, CO<sub>2</sub> adsorption for NaS-Fe and KS-Fe catalysts was mainly concentrated in the high-temperature region, corresponding to a stronger interaction with CO<sub>2</sub> molecules. Additionally, the adsorbed CO<sub>2</sub> could dissociate on the surface of the reduced iron catalysts and form CO molecules during CO<sub>2</sub>-TPD process, and the relative amount of CO to CO<sub>2</sub> desorption could serve as a reference for the ability to activate CO<sub>2</sub> [37]. The quantitative results of CO<sub>2</sub> and CO desorption in different temperature regions are given in Table S6. CO desorption in the low-temperature region (< 400 °C) was negligible for the studied catalysts (Fig. 4b), demonstrating the low reactivity of these weakly adsorbed CO<sub>2</sub> species. Under the reaction conditions of CO<sub>2</sub> hydrogenation, the strongly adsorbed CO<sub>2</sub> species should be the main reactants that could participate in the further conversion. In terms of the high-temperature region (> 400 °C), the value of CO/CO<sub>2</sub> for KS-Fe (118.7 %) was much higher than that for NaS-Fe (64.8 %), indicating that the adsorbed CO<sub>2</sub> species were more easily dissociated on KS-Fe catalyst, which undoubtedly contributed to a higher CO<sub>2</sub> conversion.

Based on CO-mediated pathway, the activation behavior of CO on catalyst surface is considered to be crucial in determining the dominant reactive species and altering the reaction network for alcohol synthesis [38]. The conversion tendency of adsorbed CO on NaS-Fe and KS-Fe catalysts was further clarified by CO-DRIFTS (Fig. 4c-d). The absorption bands at 2000–2250 cm<sup>-1</sup> and 2300–2400 cm<sup>-1</sup> correspond to the vibration of gaseous CO and CO<sub>2</sub>, respectively [39]. The gaseous CO<sub>2</sub> should be formed through the oxidation of adsorbed CO by \*O species

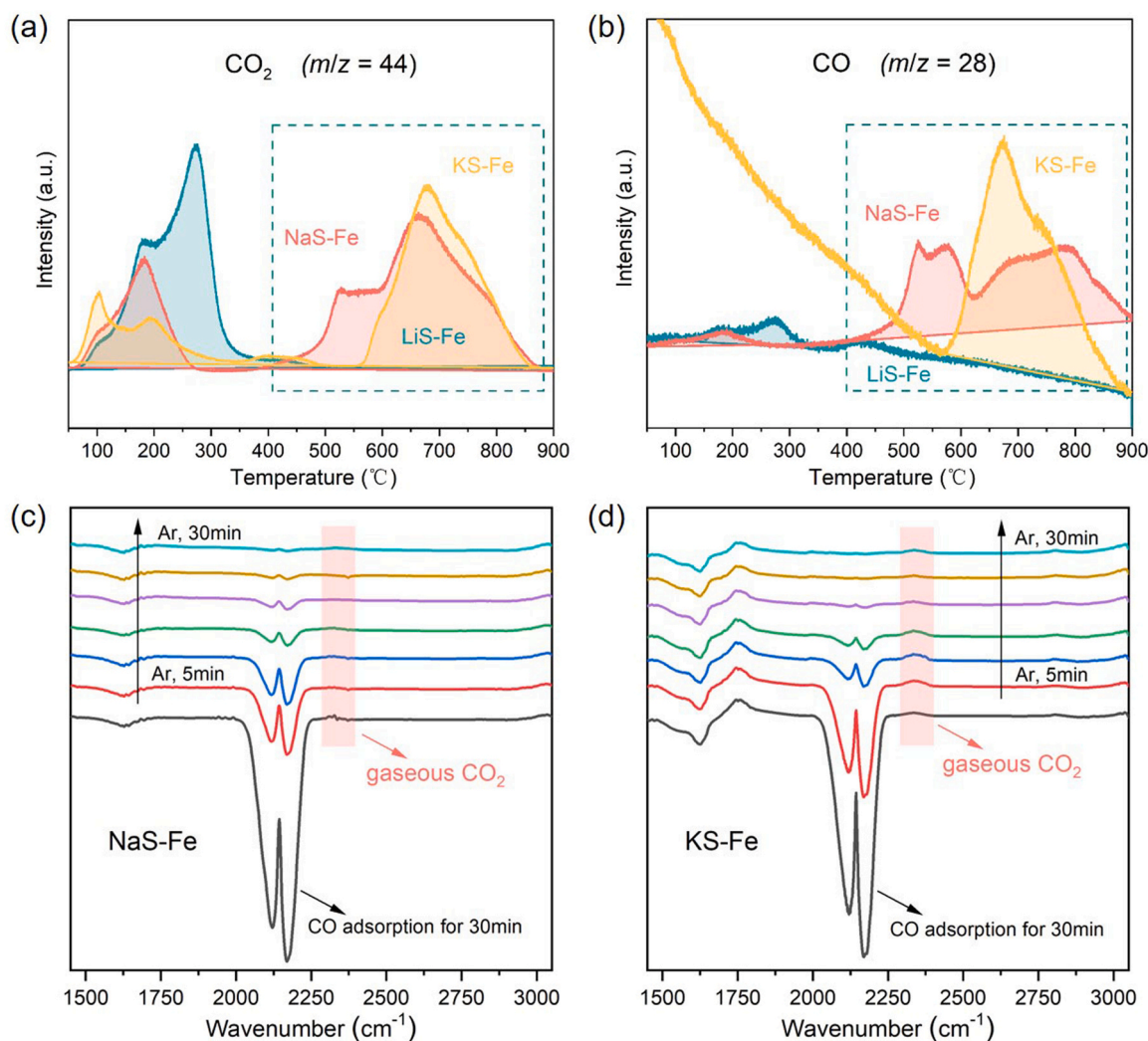


Fig. 4. MS signals of (a) CO<sub>2</sub> and (b) CO during CO<sub>2</sub>-TPD process. In situ DRIFT spectra of CO adsorption on the spent (c) NaS-Fe and (d) KS-Fe catalysts.

generated from CO dissociation [40]. Compared to NaS-Fe, the free CO<sub>2</sub> peak on KS-Fe was significantly larger and persisted throughout the entire purging process. This suggested that the adsorbed CO on KS-Fe was more likely to be dissociated, which was consistent with its low CO selectivity and high hydrocarbon selectivity (Fig. 1).

### 3.4. Structure-performance relationship

The activation behaviors toward CO<sub>2</sub>/CO and H<sub>2</sub> varied with the dual-promoter in iron catalysts and affected the steady-state phase composition during the reaction, which was critical for the formation of reactive species. As reflected by the XRD patterns (Fig. 5a), the LiS-Fe catalyst consisted mainly of Fe<sub>3</sub>O<sub>4</sub> phase after reaction process, whereas Fe<sub>5</sub>C<sub>2</sub> was the dominant phase in the spent NaS-Fe and KS-Fe catalysts. MES measurements were further conducted to obtain details of the phase composition. The Mössbauer spectra and deconvoluted sub-spectra of spent catalysts are presented (NaS-Fe in Fig. 5b, LiS-Fe in Fig. S5, KS-Fe in Fig. S6), and a direct comparison of the phase compositions is given as well (Fig. 5c, Table S7). Fe<sub>5</sub>C<sub>2</sub> and Fe<sub>3</sub>O<sub>4</sub> phases accounted for over 80 % of the iron catalysts, and the relative contents varied with the applied dual-promoters. The fraction of Fe<sub>3</sub>O<sub>4</sub> phase in LiS-Fe catalyst was as high as 78.2 %, with only 17.5 % of Fe<sub>5</sub>C<sub>2</sub> phase. Whereas, the fractions of Fe<sub>5</sub>C<sub>2</sub> phase in NaS-Fe and KS-Fe catalysts reached 71.4 % and 86.9 %, respectively. Apparently, the presence of heavier alkali metal was more conducive to the carburization of iron

catalysts during reaction. Generally, Fe<sub>3</sub>O<sub>4</sub> and Fe<sub>5</sub>C<sub>2</sub> are considered as active phases for RWGS and FTS processes, respectively, and the synergy of both phases contributes to the efficient conversion of CO<sub>2</sub> [41]. Based on the phase compositions of the iron catalysts and their catalytic performance in CO<sub>2</sub> hydrogenation, a composition-performance relationship was established (Fig. 5d). Both CO<sub>2</sub> conversion and C<sub>5+</sub> selectivity were positively correlated with the content of Fe<sub>5</sub>C<sub>2</sub>, instead of Fe<sub>3</sub>O<sub>4</sub>, hinting that Fe<sub>5</sub>C<sub>2</sub> phase should be the key factor affecting CO<sub>2</sub> activation and carbon chain growth. However, the role of Fe<sub>5</sub>C<sub>2</sub> phase in promoting C–C coupling was not reflected in the formation of C<sub>2+</sub> alcohols, as indicated by the variation in alcohol selectivity. This might have to do with the fact that alkyl–\*CO coupling was thermodynamically unfavorable compared to alkyl–alkyl coupling steps [10]. Furthermore, the catalytic property of Fe<sub>5</sub>C<sub>2</sub> phase in the studied catalysts should be different due to the distinct electronic effects of applied alkali metals [29]. Not only the content of Fe<sub>5</sub>C<sub>2</sub> phase, but also the electronic states of involved Fe sites, would exert an influence on the activation behavior of CO intermediate at the catalyst surface, and then the generation and conversion of dominant reactive species.

To probe the activity origin of iron catalysts for CO<sub>2</sub> conversion to higher alcohols, in situ XRD was conducted on NaS-Fe catalyst to complete the picture of the structural evolution during H<sub>2</sub> reduction and CO<sub>2</sub> hydrogenation. During the H<sub>2</sub> reduction process (Fig. 6a), the origin Fe<sub>2</sub>O<sub>3</sub> phase was first reduced into Fe<sub>3</sub>O<sub>4</sub>, then into metallic Fe with a small proportion of FeO, after the system temperature was maintained at

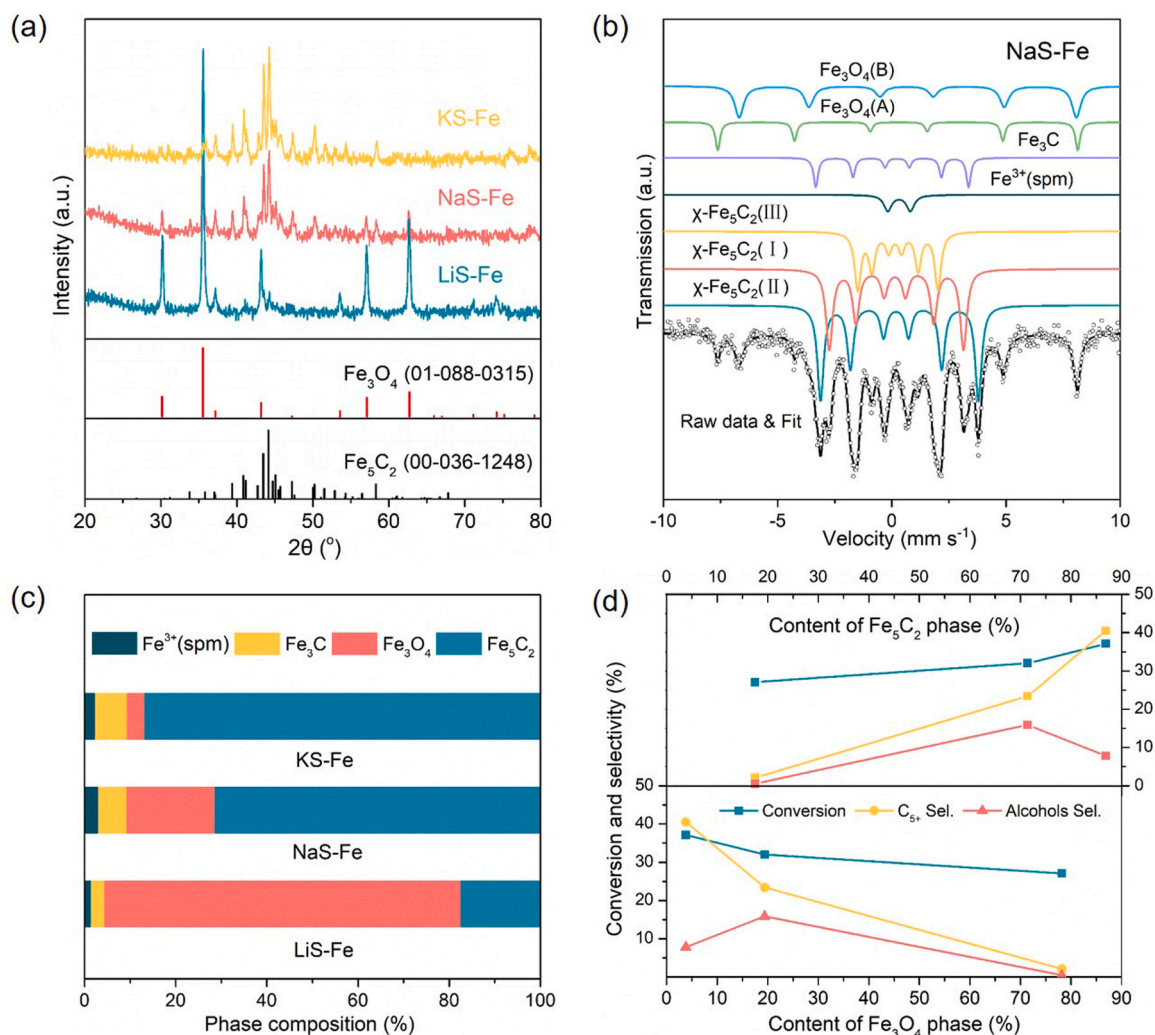


**Fig. 5.** (a) XRD patterns of spent catalysts. (b) Mössbauer spectra and deconvoluted sub-spectra of spent NaS-Fe catalyst. (c) Detailed phase composition of spent iron catalysts, as obtained from MES analysis. (d) The relationship between iron phase composition and catalytic performance in  $\text{CO}_2$  hydrogenation.

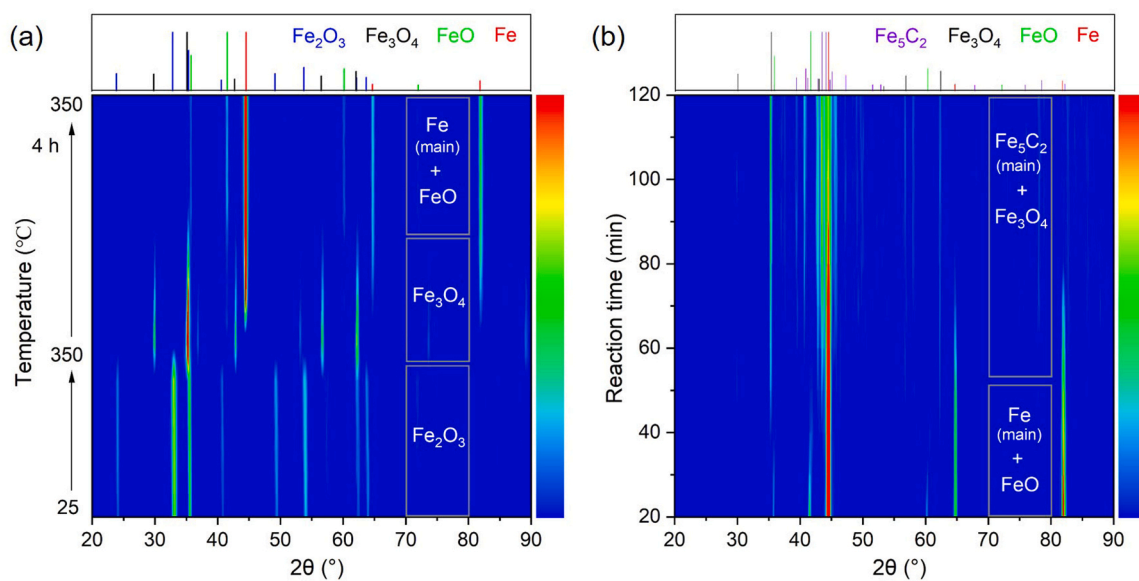


**Fig. 6.** In situ XRD patterns of NaS-Fe catalyst during (a)  $\text{H}_2$  reduction and (b) reaction processes. Reaction conditions:  $320^{\circ}\text{C}$ , 0.1 MPa,  $\text{H}_2/\text{CO}_2 = 3$ .



320 °C for 4 h. In the subsequent reaction process (Fig. 6b), the diffractions for metallic Fe and FeO became weaker and finally vanished, associated with the oxidation and carburization of the reduced iron species; the diffractions assigned to  $\text{Fe}_5\text{C}_2$  and  $\text{Fe}_3\text{O}_4$  appeared after 50 min on stream and gradually dominated the composition. This results convincingly indicated that  $\text{Fe}_5\text{C}_2$  and  $\text{Fe}_3\text{O}_4$  are indeed the dominant iron phases during reaction, and account for the catalytic conversion of  $\text{CO}_2$ . Also, these active phases could be formed within a short time from the onset of  $\text{CO}_2$  hydrogenation. Combined the results of composition-performance relationship in Fig. 5, the electronic promoters of Na and sulfate mainly exerted influence on  $\text{Fe}_5\text{C}_2$  phase and then altered the reaction network for alcohol synthesis.

Considering the significance of the electronic states of metal sites in surface activation behaviors, XPS characterization was performed to gain insights into the difference of Fe sites in the studied catalysts. The fresh catalysts showed no difference in the peak position of Fe 2p despite different alkali metal promoters (Fig. 7a), likely due to the low contents of the promoters. Phase transformation and element redistribution occurred during  $\text{CO}_2$  hydrogenation process, and the difference between the electronic states of Fe sites in the catalysts became apparent (Fig. 7b). The Fe 2p peaks at about 710 eV correspond to iron oxides ( $\text{FeO}_x$ ) on the surface, and the peaks at about 707 eV are attributed to iron carbides ( $\text{FeC}_x$ ) [41–43]. Unlike LiS-Fe catalyst, a clear and independent characteristic peak of Fe  $2p_{3/2}$  for iron carbides appeared for NaS-Fe and KS-Fe catalysts, in line with the positive role of Na and K in

the formation and stabilization of iron carbides [44]. Additionally, the Fe  $2p_{3/2}$  peak featuring  $\text{FeC}_x$  phase in KS-Fe catalyst shifted to a lower binding energy than that in NaS-Fe catalyst, indicating the much easier electron transfer from heavier alkali metal to Fe. Based on the knowledge of C–O bond activation on transition metals, the difference in CO activation was expected among the studied catalysts, due to the varied electronic states of Fe sites in  $\text{FeC}_x$  phase [23]. The  $\text{Fe}_5\text{C}_2$  phase in KS-Fe catalyst, with more electron-rich Fe centers, was expected to catalyze CO dissociation directly and generate abundant alkyl species. Alkyl–alkyl coupling was thus favored during the reaction, while the chance of alkyl–\*CO coupling was diminished, leading to reduced production of higher alcohols. In contrast, the alkali metal Na, with moderate electronic effects, would not entirely counteract the opposite electronic effects of sulfate, which was more suitable for site regulation for non-dissociated CO activation. Meanwhile, the presence of Na could ensure the basic need for CO dissociation and C–C coupling, which was simply not enough when relying on the metal Li. Na-S modification was proven suitable for iron catalysts to construct necessary sites for HAS, and the advantage of Na should lie on its effective and moderate electronic effects. Furthermore, the phase composition and electronic states of NaS-Fe catalyst after 8 h and 50 h of reaction were compared to investigate the changes over time. The fraction of  $\text{Fe}_5\text{C}_2$  increased from 71.4 % to 83.1 % with the prolonging of reaction time (Fig. S7, Table S7), and no apparent change was observed in the Fe 2p spectra (Fig. S8), which reasonably explained the stable alcohol production

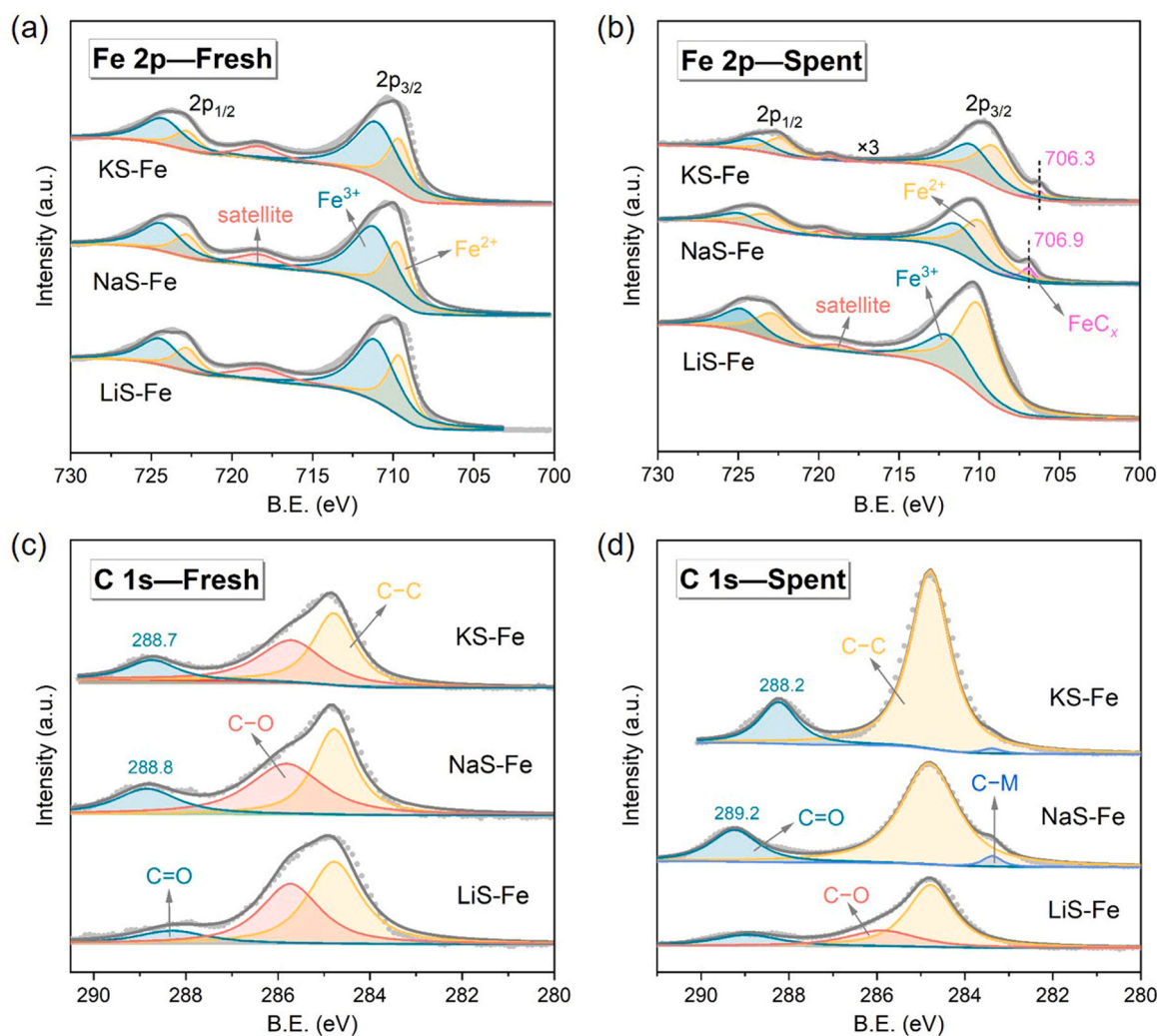


**Fig. 7.** XPS spectra of Fe 2p for (a) fresh and (b) spent catalysts, C 1s for (c) fresh and (d) spent catalysts. The XPS survey and corresponding spectra of O 1 s, S 2p, and alkali metals were given in Figs. S9–14.

during the reaction process (Fig. S3).

In addition, C 1 s spectra could also provide insights into the impact of dual-promoters on CO<sub>2</sub> activation. The deconvoluted C 1s spectra for fresh catalysts exhibited three main spectral regions (Fig. 7c), including C–C bond (284.8 eV), C–O bond (285.5–285.8 eV), and C=O bond in chemisorbed CO<sub>2</sub> or carbonate (288–289 eV) [39,45]. Upon reaction, the peak position and relative intensity varied in different degrees, especially the spectral peak for C=O bond (Fig. 7d). The small peak for C=O bond in LiS-Fe catalyst was consistent with the weak CO<sub>2</sub> adsorption in CO<sub>2</sub>-TPD results (Fig. 4a). Note that the peak for C=O bond in NaS-Fe catalyst shifted towards higher binding energy after reaction (288.8→289.2 eV), whereas that for KS-Fe catalyst shifted towards lower binding energy (288.7→288.2 eV). It was indicated that the sulfate exerted a greater influence on the electronic environment of Fe sites in NaS-Fe catalyst, whereas the influence of K was more prominent in KS-Fe, which diminished the regulatory role of sulfate. This finding further demonstrated that Na-S dual-promoter was more suitable to regulate the property of iron catalyst and meet the requirements for HAS.

### 3.5. Reaction mechanism

In situ high-pressure DRIFT measurement was conducted on NaS-Fe catalyst under realistic condition (320 °C, 1.0 MPa, H<sub>2</sub>/CO<sub>2</sub>/N<sub>2</sub> = 72/24/4) to monitor the key surface intermediates during CO<sub>2</sub> hydrogenation reaction (Fig. 8). The IR bands associated with carbonate (1455 and 1505 cm<sup>-1</sup> for \*CO<sub>3</sub>, 1471 and 1715 cm<sup>-1</sup> for \*HCO<sub>3</sub>) and formate (1557 and 1372 cm<sup>-1</sup>) species appeared upon the introduction of CO<sub>2</sub>/H<sub>2</sub> and gradually intensified, which represented the adsorption and activation of CO<sub>2</sub> reactant on catalyst surface [46,47]. The stretching vibrations of gaseous CO at 2113 and 2178 cm<sup>-1</sup> were observed immediately, indicating that RWGS between the carbonate/formate species with H<sub>2</sub> should be an initial process for CO<sub>2</sub> hydrogenation [48, 49]. The IR peaks at 1304 and 3016 cm<sup>-1</sup> assigned to the stretching vibrations of C–H bond in CH<sub>4</sub> appeared at an early stage and intensified as the reaction process, suggesting the tendency of adsorbed CO species to be dissociated and hydrogenated. The intensity of all the IR bands almost reached a steady-state value after the system was maintained at 320 °C and 1.0 MPa for 30 min. The bending vibrations of C–H bond in –CH– (1340 cm<sup>-1</sup>), –CH<sub>2</sub>– (1465 cm<sup>-1</sup>), and –CH<sub>3</sub> (1380,

1460 cm<sup>-1</sup>) confirmed the presence of reactive alkyl species, which provided opportunity for C–C coupling to C<sub>2+</sub> products [47,50]. The IR peaks corresponding to the stretching vibrations of C=C (1656 cm<sup>-1</sup>) and C–H (3050–3150 cm<sup>-1</sup>) in unsaturated hydrocarbons, was in good accordance with the massive formation of olefins on NaS-Fe catalyst during CO<sub>2</sub> hydrogenation (Table S2) [38]. The linear CO adsorption band (2078 cm<sup>-1</sup>) was assigned to the non-dissociative \*CO species, which were considered to be important intermediates for alcohol formation via the insertion steps with alkyl species. In addition, the emergence of adsorbed \*CH<sub>3</sub>CHO (stretching vibrations of C–H at 2865 cm<sup>-1</sup> and C=O at 1749 cm<sup>-1</sup>) and CH<sub>3</sub>CH<sub>2</sub>O\* (asymmetric and symmetric stretching of C–H at 2968 and 2876 cm<sup>-1</sup>) species, provided further evidence for the coupling reactions between alkyl and \*C(H)O species, as well as the subsequent hydrogenation towards alcohols [13, 38,50]. Furthermore, the dominant reaction pathways under Li-S and K-S promotion have also been verified. The strong tendency for hydrogenated termination over LiS-Fe catalyst was deeply supported by the much stronger IR signals of CH<sub>4</sub> (Fig. S15). As for KS-Fe catalyst, the IR peaks at 2800–3000 cm<sup>-1</sup> assigned to the stretching vibrations of saturated C–H bond were quite prominent compared with other species (Fig. S16), which provided evidence for the massive formation of hydrocarbons through C–C coupling between alkyl species.

DFT calculations were further performed to gain an atomic level understanding of the difference in alcohol production over the iron catalysts. Three Fe<sub>5</sub>C<sub>2</sub>(510) models decorated with sulfate and an alkali metal (Li, Na, K) were established to represent the different modified iron catalysts. Generally, the coupling between \*CO and alkyl species was the essential step to form the precursors of alcohol products in CO<sub>2</sub> hydrogenation. Considering \*CH<sub>2</sub> was the primary alkyl specie during the reaction and ethanol was the main alcohol product, the coupling of \*CH<sub>2</sub> and \*CO was taken as probing reaction to investigate the activity for selective C–C coupling (Figs. S17–19). For Na-S/Fe<sub>5</sub>C<sub>2</sub>(510) model, the \*CH<sub>2</sub>–\*CO coupling required a lower activation energy of 0.53 eV than K-S/Fe<sub>5</sub>C<sub>2</sub>(510) (0.62 eV) and Li-S/Fe<sub>5</sub>C<sub>2</sub>(510) (0.85 eV) models (Fig. 9a). This indicated that \*CH<sub>2</sub>–\*CO coupling was more favorable on the Na-S modified iron catalyst. In addition, CO adsorption behavior on the three models was also evaluated (Fig. 9b and Fig. S20). The K-S/Fe<sub>5</sub>C<sub>2</sub>(510) model delivered a stronger CO adsorption capacity with the adsorption energy (*E*<sub>ads</sub>) of –2.55 eV, whereas Li-S/Fe<sub>5</sub>C<sub>2</sub>(510) and Na-S/Fe<sub>5</sub>C<sub>2</sub>(510) possessed weak and moderate CO adsorption strengths

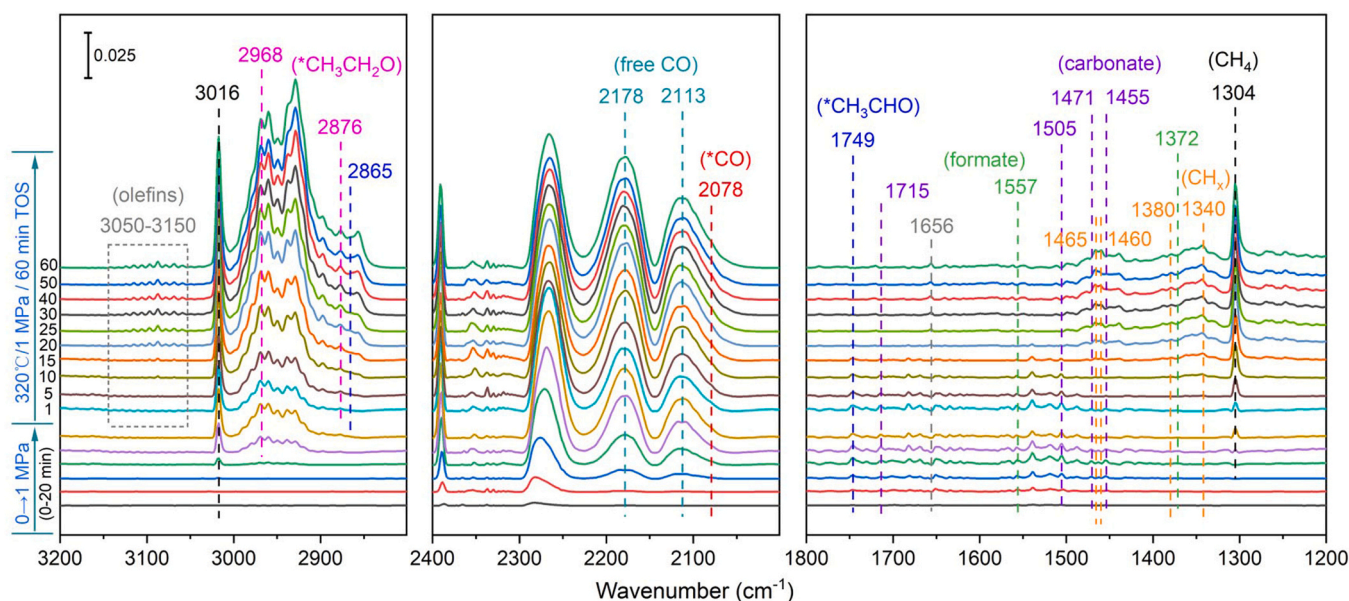


**Fig. 8.** In situ DRIFT spectra for CO<sub>2</sub> hydrogenation over NaS-Fe catalyst. The spectra were collected during the pressurizing and reaction process. Reaction conditions: 320 °C, 1.0 MPa, H<sub>2</sub>/CO<sub>2</sub>/N<sub>2</sub> = 72/24/4.

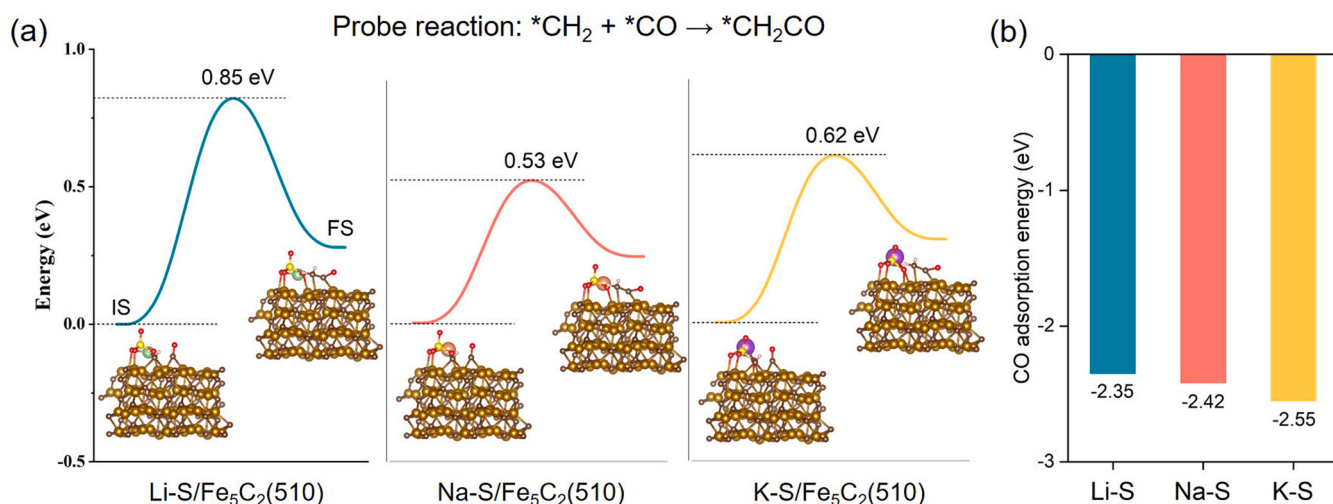


**Fig. 9.** DFT calculations on (a)  $^*\text{CH}_2$ - $^*\text{CO}$  coupling and (b) CO adsorption on different modified  $\text{Fe}_5\text{C}_2(510)$  models. K atom (purple), Na atom (orange), Li atom (green), Fe atom (dark yellow), S atom (yellow), C atom (brown), O atom (red), and H (white) in the profiles.

with the  $E_{\text{ads}}$  of  $-2.35$  and  $-2.42$  eV, respectively. The strong CO adsorption was often accompanied by incidental C–O dissociation and contributed mainly to the formation of hydrocarbons, as the KS-Fe catalyst behaved in  $\text{CO}_2$  hydrogenation. Conversely, the weak CO adsorption would decrease the reactivity of CO on catalyst surface and give a higher CO byproduct selectivity, which was consistent with the product distribution of LiS-Fe catalyst. These results were in line with the catalytic performance of the studied catalysts and also supported the importance of moderate CO adsorption for HAS from  $\text{CO}_2$  hydrogenation.

On the basis of the above discussion, the relationship between catalyst properties and higher alcohols synthesis was better understood. The key point of catalyst design is to accelerate alkyl- $^*\text{CO}$  coupling steps towards higher alcohols. In terms of iron catalysts,  $\text{Fe}_5\text{C}_2$  phase plays a key role in activating  $\text{CO}_2/\text{CO}$  and catalyzing C–C coupling, and the catalytic property of involved Fe sites varies depending on the surrounding electronic environment. The presence of sulfate and alkali metal, with different electronic effects and spatial distribution, helps to regulate the Fe sites with distinct electronic properties, which is expected to cover the multiple catalytic functions required for HAS. Generally, the electron-rich Fe sites tend to catalyze the dissociation of adsorbed CO and generate alkyl species, whereas the relatively electron-deficient Fe sites are more favorable for non-dissociated CO activation.

Li-S modification made no significant contribution to CO activation and C–C coupling on iron catalyst, whereas the hydrogenation ability was strengthened, leading to massive  $\text{CH}_4$  formation. The electronic effects of K significantly diminished the regulatory role of sulfate, and electron-rich Fe sites were dominant in KS-Fe catalyst. As a result, alkyl-alkyl coupling dominated in the reaction network and contributed mainly to the formation of hydrocarbons. In contrast, Na-S modification ensured sufficient ability for CO dissociation, meanwhile, the sulfate species could function normally in regulating the electronic property of surrounding Fe sites. A better balance among the catalytic sites for CO dissociation, non-dissociated CO activation, and hydrogenated termination, was achieved by Na-S modification in iron catalyst, which consequently optimized the reaction pathways toward higher alcohols. This advantage was ascribed to the moderate electronic effects of Na as compared with Li and K (Fig. 10).

#### 4. Conclusion

In summary, modifying the iron catalyst with alkali metal and sulfate, is a potential way to regulate the catalytic property and meet the requirements for higher alcohols synthesis. The alkali metal Na, with moderate electronic effects, was proven suitable to cooperate with sulfate to construct required multiple catalytic sites in iron catalyst. The

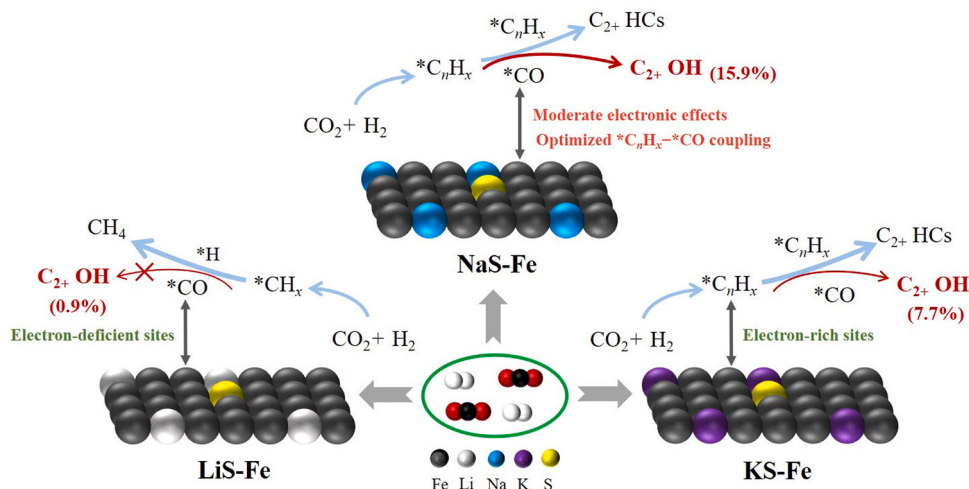


**Fig. 10.** Schematic of  $\text{CO}_2$  hydrogenation to higher alcohols over iron catalysts.



fine-tuning of iron catalyst with Na-S dual-promoter enabled a better balance among CO dissociation, non-dissociated CO activation, and hydrogenated termination, which was conducive to the key step of alkyl-\*CO coupling towards alcohol formation. The NaS-Fe catalyst achieved a CO<sub>2</sub> conversion of 32.0 % and a C<sub>2+</sub>OH yield of 78.5 mg g<sub>cat</sub><sup>-1</sup> h<sup>-1</sup>. In contrast, Li-S modification was insufficient for C–C coupling and necessary hydrogenation inhibition, and the presence of K would counteract the role of sulfate in regulating the electronic property of iron sites and mainly contribute to CO dissociation. The observations confirm the importance of local electronic modification of metal sites for catalytic performance. Furthermore, the combination of sulfate and alkali metal, constitutes a general strategy to tune the electronic states of metal sites and corresponding catalytic function, providing more flexibility in site regulation for targeted synthesis.

## CRediT authorship contribution statement

**Yang Yu:** Investigation. **Bin Wu:** Investigation. **Jian Wei:** Writing – review & editing, Supervision, Formal analysis, Funding acquisition, Methodology. **Congming Li:** Writing – review & editing, Supervision, Funding acquisition, Methodology. **Qinqin Niu:** Investigation. **Na Liu:** Investigation. **Qingjie Ge:** Writing – review & editing, Supervision, Conceptualization, Funding acquisition, Methodology. **Ruwei Yao:** Writing – review & editing, Writing – original draft, Project administration, Methodology, Investigation, Formal analysis, Conceptualization, Funding acquisition.

## Declaration of Competing Interest

The authors declare that they have no known competing financial interests or personal relationships that could have appeared to influence the work reported in this paper.

## Data availability

Data will be made available on request.

## Acknowledgements

The authors would like to thank the support of National Natural Science Foundation of China (22202150, 22372165), Fundamental Research Program of Shanxi Province (202203021212232), Key Research and Development Program of Shanxi Province (202202090301013), and the Youth Innovation Promotion Association of the Chinese Academy of Sciences (2020189).

## Appendix A. Supporting information

Supplementary data associated with this article can be found in the online version at [doi:10.1016/j.apcatb.2024.124159](https://doi.org/10.1016/j.apcatb.2024.124159).

## References

- [1] L. Wang, E. Guan, Y. Wang, L. Wang, Z. Gong, Y. Cui, X. Meng, B.C. Gates, F. S. Xiao, Silica accelerates the selective hydrogenation of CO<sub>2</sub> to methanol on cobalt catalysts, *Nat. Commun.* 11 (2020) 1033.
- [2] B.Z. Yao, T.C. Xiao, O.A. Makgae, X.Y. Jie, S. Gonzalez-Cortes, S.L. Guan, A. I. Kirkland, J.R. Dilworth, H.A. Al-Megren, S.M. Alshihri, P.J. Dobson, G.P. Owen, J.M. Thomas, P.P. Edwards, Transforming carbon dioxide into jet fuel using an organic combustion-synthesized Fe-Mn-K catalyst, *Nat. Commun.* 11 (2020) 6395.
- [3] X.Z. Shao, X.F. Yang, J.M. Xu, S. Liu, S. Miao, X.Y. Liu, X. Su, H.M. Duan, Y. Q. Huang, T. Zhang, Iridium single-atom catalyst performing a quasi-homogeneous hydrogenation transformation of CO<sub>2</sub> to formate, *Chem* 5 (2019) 693–705.
- [4] P.S. Li, J.H. Bi, J.Y. Liu, Q.G. Zhu, C.J. Chen, X.F. Sun, J.L. Zhang, B.X. Han, In situ dual doping for constructing efficient CO<sub>2</sub>-to-methanol electrocatalysts, *Nat. Commun.* 13 (2022) 1965.
- [5] L.P. Ding, T.T. Shi, J. Gu, Y. Cui, Z.Y. Zhang, C.J. Yang, T. Chen, M. Lin, P. Wang, N.H. Xue, L.M. Peng, X.F. Guo, Y. Zhu, Z.X. Chen, W.P. Ding, CO<sub>2</sub> hydrogenation to ethanol over Cu@Na-Beta, *Chem* 6 (2020) 2673–2689.
- [6] D. Goud, S.R. Churipard, D. Bagchi, A.K. Singh, M. Riyaz, C.P. Vinod, S.C. Peter, Strain-enhanced phase transformation of iron oxide for higher alcohol production from CO<sub>2</sub>, *ACS Catal.* 12 (2022) 11118–11128.
- [7] J. Chen, Y. Zha, B. Liu, Y. Li, Y. Xu, X. Liu, Rationally designed water enriched nano reactor for stable CO<sub>2</sub> hydrogenation with near 100% ethanol selectivity over diatomic palladium active sites, *ACS Catal.* 13 (2023) 7110–7121.
- [8] H.S. Jung, B.G. Kim, J.W. Bae, Synthetic routes of clean hydrocarbons fuels and oxygenates by catalytic conversions of carbon oxides, *Appl. Catal. B* 343 (2024) 123477.
- [9] F. Zeng, C. Mebrahtu, X.Y. Xi, L.F. Liao, J. Ren, J.X. Xie, H.J. Heeres, R. Palkovits, Catalysts design for higher alcohols synthesis by CO<sub>2</sub> hydrogenation: Trends and future perspectives, *Appl. Catal. B* 291 (2021) 120073.
- [10] Y. Sheng, M.V. Polynski, M.K. Eswaran, B. Zhang, A.M.H. Lim, L. Zhang, J. Jiang, W. Liu, S.M. Kozlov, A review of mechanistic insights into CO<sub>2</sub> reduction to higher alcohols for rational catalyst design, *Appl. Catal. B* 343 (2024) 123550.
- [11] D. Xu, Y.Q. Wang, M.Y. Ding, X.L. Hong, G.L. Liu, S.C.E. Tsang, Advances in higher alcohol synthesis from CO<sub>2</sub> hydrogenation, *Chem* 7 (2021) 849–881.
- [12] D. Xu, M. Ding, X. Hong, G. Liu, Mechanistic aspects of the role of K promotion on Cu-Fe-based catalysts for higher alcohol synthesis from CO<sub>2</sub> hydrogenation, *ACS Catal.* 10 (2020) 14516–14526.
- [13] D. Xu, M.Y. Ding, X.L. Hong, G.L. Liu, S.C.E. Tsang, Selective C<sub>2+</sub> alcohol synthesis from direct CO<sub>2</sub> hydrogenation over a Cs-promoted Cu-Fe-Zn catalyst, *ACS Catal.* 10 (2020) 5250–5260.
- [14] T.T. Qin, T.J. Lin, X.Z. Qi, C.Q. Wang, L.S. Li, Z.Y. Tang, L.S. Zhong, Y.H. Sun, Tuning chemical environment and synergistic relay reaction to promote higher alcohols synthesis via syngas conversion, *Appl. Catal. B* 285 (2021) 119840.
- [15] Y.W. Li, W. Gao, M. Peng, J.B. Zhang, J. Sun, Y. Xu, S. Hong, X. Liu, X.W. Liu, M. Wei, B.S. Zhang, D. Ma, Interfacial Fe<sub>3</sub>C<sub>2</sub>-Cu catalysts toward low-pressure syngas conversion to long-chain alcohols, *Nat. Commun.* 11 (2020) 61.
- [16] S. Liu, C. Yang, S. Zha, D. Sharapa, F. Studt, Z.J. Zhao, J. Gong, Moderate surface segregation promotes selective ethanol production in CO<sub>2</sub> hydrogenation reaction over CoCu catalysts, *Angew. Chem. Int. Ed.* 61 (2021) e202109027.
- [17] H.T. Luk, C. Mondelli, S. Mitchell, S. Siol, J.A. Stewart, D. Curulla Ferré, J. Pérez-Ramírez, Role of carbonaceous supports and potassium promoter on higher alcohols synthesis over copper-iron catalysts, *ACS Catal.* 8 (2018) 9604–9618.
- [18] T. Liu, D. Xu, M. Song, X. Hong, G. Liu, K-ZrO<sub>2</sub> interfaces boost CO<sub>2</sub> hydrogenation to higher alcohols, *ACS Catal.* 13 (2023) 4667–4674.
- [19] Q. Zhang, S. Wang, R. Geng, P.F. Wang, M. Dong, J.G. Wang, W.B. Fan, Hydrogenation of CO<sub>2</sub> to higher alcohols on an efficient Cr-modified CuFe catalyst, *Appl. Catal. B* 337 (2023) 123013.
- [20] H. Yang, Y. Dang, X. Cui, X. Bu, J. Li, S. Li, Y. Sun, P. Gao, Selective synthesis of olefins via CO<sub>2</sub> hydrogenation over transition-metal-doped iron-based catalysts, *Appl. Catal. B* 321 (2023) 122050.
- [21] X. Xi, F. Zeng, H. Zhang, X. Wu, J. Ren, T. Bisswanger, C. Stampfer, J.P. Hofmann, R. Palkovits, H.J. Heeres, CO<sub>2</sub> hydrogenation to higher alcohols over K-promoted bimetallic Fe-In catalysts on a Ce-ZrO<sub>2</sub> support, *ACS Sustain. Chem. Eng.* 9 (2021) 6235–6249.
- [22] Y. Xu, P. Zhai, Y. Deng, J. Xie, X. Liu, S. Wang, D. Ma, Highly selective olefin production from CO<sub>2</sub> hydrogenation on iron catalysts: a subtle synergy between manganese and sodium additives, *Angew. Chem. Int. Ed.* 59 (2020) 21736–21744.
- [23] D.G. Miller, M. Moskovits, A study of the effects of potassium addition to supported iron catalysts in the Fischer-Tropsch reaction, *J. Phys. Chem.* 92 (1988) 6081–6085.
- [24] R.W. Yao, J. Wei, Q.J. Ge, J. Xu, Y. Han, Q.X. Ma, H.Y. Xu, J. Sun, Monometallic iron catalysts with synergistic Na and S for higher alcohols synthesis via CO<sub>2</sub> hydrogenation, *Appl. Catal. B* 298 (2021) 120556.
- [25] D. Xu, H.Q. Yang, X.L. Hong, G.L. Liu, S.C.E. Tsang, Tandem catalysis of direct CO<sub>2</sub> hydrogenation to higher alcohols, *ACS Catal.* 11 (2021) 8978–8984.
- [26] M. Ao, G.H. Pham, J. Sunarso, M.O. Tade, S.M. Liu, Active centers of catalysts for higher alcohol synthesis from syngas: a review, *ACS Catal.* 8 (2018) 7025–7050.
- [27] S. Liu, Y. He, W. Fu, J. Chen, J. Ren, L. Liao, R. Sun, Z. Tang, C. Mebrahtu, F. Zeng, Hetero-site cobalt catalysts for higher alcohols synthesis by CO<sub>2</sub> hydrogenation: A review, *J. CO<sub>2</sub> Util.* 67 (2023) 102322.
- [28] C. Huang, C. Zhu, M. Zhang, J. Chen, K. Fang, Design of efficient ZnO/ZrO<sub>2</sub> modified CuCoAl catalysts for boosting higher alcohol synthesis in syngas conversion, *Appl. Catal. B* 300 (2022) 120739.
- [29] Q. Yang, V.A. Kondratenko, S.A. Petrov, D.E. Doronkin, E. Saraçi, H. Lund, A. Arinchtin, R. Kraehnert, A.S. Skrypnik, A.A. Matvienko, E.V. Kondratenko, Identifying performance descriptors in CO<sub>2</sub> hydrogenation over iron-based catalysts promoted with alkali metals, *Angew. Chem. Int. Ed.* 61 (2022) e202116517.
- [30] M. Ao, G.H. Pham, J. Sunarso, F.P. Li, Y. Jin, S.M. Liu, Effects of alkali promoters on tri-metallic Co-Ni-Cu-based perovskite catalyst for higher alcohol synthesis from syngas, *Catal. Today* 355 (2020) 26–34.
- [31] S. Yang, H.J. Chun, S. Lee, S.J. Han, K.Y. Lee, Y.T. Kim, Comparative study of olefin production from CO and CO<sub>2</sub> using Na- and K-promoted zinc ferrite, *ACS Catal.* 10 (2020) 10742–10759.
- [32] J.D. Jiang, C.Y. Wen, Z.P. Tian, Y.C. Wang, Y.P. Zhai, L.G. Chen, Y.P. Li, Q.Y. Liu, C.G. Wang, L.L. Ma, Manganese-promoted Fe<sub>3</sub>O<sub>4</sub> microsphere for efficient conversion of CO<sub>2</sub> to light olefins, *Ind. Eng. Chem. Res.* 59 (2020) 2155–2162.
- [33] J. Wei, R.W. Yao, Y. Han, Q.J. Ge, J. Sun, Towards the development of the emerging process of CO<sub>2</sub> heterogeneous hydrogenation into high-value unsaturated heavy hydrocarbons, *Chem. Soc. Rev.* 50 (2021) 10764–10805.
- [34] C. Zhang, M. Xu, Z. Yang, M. Zhu, J. Gao, Y.-F. Han, Uncovering the electronic effects of zinc on the structure of Fe<sub>3</sub>C<sub>2</sub>-ZnO catalysts for CO<sub>2</sub> hydrogenation to linear  $\alpha$ -olefins, *Appl. Catal. B* 295 (2021) 120287.

- [35] J. Xu, J. Wei, J.X. Zhang, R.W. Yao, Q.J. Ge, Q.X. Ma, J. Sun, Highly selective production of long-chain aldehydes, ketones or alcohols via syngas at a mild condition, *Appl. Catal. B* 307 (2022) 121155.
- [36] R.W. Yao, J. Wei, Q.J. Ge, J. Xu, Y. Han, H.Y. Xu, J. Sun, Structure sensitivity of iron oxide catalyst for CO<sub>2</sub> hydrogenation, *Catal. Today* 371 (2021) 134–141.
- [37] Z.Y. Wang, C.S. Yang, X.H. Li, X.W. Song, C.L. Pei, Z.J. Zhao, J.L. Gong, The role of CO<sub>2</sub> dissociation in CO<sub>2</sub> hydrogenation to ethanol on CoCu/silica catalysts, *Nano Res.* 16 (2023) 6128–6133.
- [38] Y. Wang, W. Wang, R. He, M. Li, J. Zhang, F. Cao, J. Liu, S. Lin, X. Gao, G. Yang, M. Wang, T. Xing, T. Liu, Q. Liu, H. Hu, N. Tsubaki, M. Wu, Carbon-based electron buffer layer on ZnO<sub>x</sub>–Fe<sub>3</sub>C<sub>2</sub>–Fe<sub>3</sub>O<sub>4</sub> boosts ethanol synthesis from CO<sub>2</sub> hydrogenation, *Angew. Chem. Int. Ed.* 62 (2023) e202311786.
- [39] M. Irshad, H.-J. Chun, M.K. Khan, H. Jo, S.K. Kim, J. Kim, Synthesis of n-butanol-rich C<sub>3+</sub> alcohols by direct CO<sub>2</sub> hydrogenation over a stable Cu–Co tandem catalyst, *Appl. Catal. B* 340 (2024) 123201.
- [40] B. Liu, W. Li, J. Zheng, Q. Lin, X. Zhang, J. Zhang, F. Jiang, Y. Xu, X. Liu, CO<sub>2</sub> formation mechanism in Fischer–Tropsch synthesis over iron-based catalysts: a combined experimental and theoretical study, *Catal. Sci. Technol.* 8 (2018) 5288–5301.
- [41] J. Zhu, P. Wang, X. Zhang, G. Zhang, R. Li, W. Li, T.P. Senftle, W. Liu, J. Wang, Y. Wang, A. Zhang, Q. Fu, C. Song, X. Guo, Dynamic structural evolution of iron catalysts involving competitive oxidation and carburization during CO<sub>2</sub> hydrogenation, *Sci. Adv.* 8 (2022) eabm3629.
- [42] S. Ahmed, M. Irshad, W. Yoon, N. Karanwal, J.R. Sugiarto, M.K. Khan, S.K. Kim, J. Kim, Evaluation of MgO as a promoter for the hydrogenation of CO<sub>2</sub> to long-chain hydrocarbons over Fe-based catalysts, *Appl. Catal. B* 338 (2023) 123052.
- [43] C. Qin, Y.X. Du, K. Wu, Y.F. Xu, R. Li, H.F. Fan, D. Xu, M.Y. Ding, Facet-controlled Cu-doped and K-promoted Fe<sub>2</sub>O<sub>3</sub> nanosheets for efficient CO<sub>2</sub> hydrogenation to liquid hydrocarbons, *Chem. Eng. J.* 467 (2023) 143403.
- [44] H.Z. Wang, X.W. Nie, Y. Liu, M.J. Janik, X.P. Han, Y.D. Deng, W.B. Hu, C.S. Song, X.W. Guo, Mechanistic insight into hydrocarbon synthesis via CO hydrogenation on  $\gamma$ -Fe<sub>5</sub>C<sub>2</sub> catalysts, *ACS Appl. Mater. Interfaces* 14 (2022) 37637–37651.
- [45] M. Favaro, H. Xiao, T. Cheng, W.A. Goddard, J. Yano, E.J. Crumlin, Subsurface oxide plays a critical role in CO<sub>2</sub> activation by Cu(111) surfaces to form chemisorbed CO<sub>2</sub>, the first step in reduction of CO<sub>2</sub>, *PNAS* 114 (2017) 6706–6711.
- [46] M.G. Sibi, M.K. Khan, D. Verma, W. Yoon, J. Kim, High-yield synthesis of BTEX over Na–FeAlO<sub>x</sub>/Zn–HZSM-5@SiO<sub>2</sub> by direct CO<sub>2</sub> conversion and identification of surface intermediates, *Appl. Catal. B* 301 (2022) 120813.
- [47] J. Wang, T. Wang, Y. Xi, G. Gao, P. Sun, F. Li, In-situ-formed potassium-modified nickel-zinc carbide boosts production of higher alcohols beyond CH<sub>4</sub> in CO<sub>2</sub> hydrogenation, *Angew. Chem. Int. Ed.* 62 (2023) e202311335.
- [48] M.K. Khan, P. Butolia, H. Jo, M. Irshad, D. Han, K.-W. Nam, J. Kim, Selective conversion of carbon dioxide into liquid hydrocarbons and long-chain  $\alpha$ -olefins over Fe-amorphous AlO<sub>x</sub> bifunctional catalysts, *ACS Catal.* 10 (2020) 10325–10338.
- [49] X.Z. Qi, T.J. Lin, Y.L. An, X.X. Wang, D. Lv, Z.Y. Tang, L.S. Zhong, Regulating oxygen vacancies for enhanced higher oxygenate synthesis via syngas, *ACS Catal.* 13 (2023) 11566–11579.
- [50] Z. Zeng, Z. Li, L. Kang, X. Han, Z. Qi, S. Guo, J. Wang, A. Rykov, J. Lv, Y. Wang, X. Ma, A monodisperse  $\epsilon'$ -(Co<sub>x</sub>Fe<sub>1-x</sub>)<sub>2</sub>C bimetallic carbide catalyst for direct conversion of syngas to higher alcohols, *ACS Catal.* 12 (2022) 6016–6028.